Biol Cybern (2010) 103:433–446
DOI 10.1007/s00422-010-0414-6

ORIGINAL PAPER

Biological Cybernetics

Non-directional motion detectors can be used to mimic optic flow dependent behaviors

Jonathan P. Dyhr · Charles M. Higgins

Received: 26 January 2010 / Accepted: 19 November 2010 / Published online: 16 December 2010

Abstract Insect navigational behaviors including obstacle avoidance, grazing landings, and visual odometry are dependent on the ability to estimate flight speed based only on visual cues. In honeybees, this visual estimate of speed is largely independent of both the direction of motion and the spatial frequency content of the image. Electrophysiological recordings from the motion-sensitive cells believed to underlie these behaviors have long supported spatio-temporally tuned correlation-type models of visual motion detection whose speed tuning changes as the spatial frequency of a stimulus is varied. The result is an apparent conflict between behavioral experiments and the electrophysiological and modeling data. In this article, we demonstrate that conventional correlation-type models are sufficient to reproduce some of the speed-dependent behaviors observed in honeybees when square wave gratings are used, contrary to the theoretical predictions. However, these models fail to match the behavioral observations for sinusoidal stimuli. Instead, we show that non-directional motion detectors, which underlie the correlation-based computation of directional motion, can be used to mimic these same behaviors even when narrowband gratings are used. The existence of such non-directional motion detectors is supported both anatomically and electrophysiologically, and they have been hypothesized to be critical in the Dipteran elementary motion detector (EMD) circuit.

Keywords Vision · Optic flow · Motion detection · Speed estimation · Computational modeling

J. P. Dyhr (✉) · C. M. Higgins
Department of Neuroscience, The University of Arizona,
1040 E. 4th Street, Tucson, AZ 85721-0077, USA
e-mail: jdyhr@u.washington.edu

Present Address:
J. P. Dyhr
Department of Biology,
The University of Washington,
24 Kincaid Hall, Seattle,
WA 98195-1800, USA

C. M. Higgins
Department of Electrical and Computer Engineering,
The University of Arizona, Tucson, AZ, USA

1 Introduction

The pioneering work of Karl von Frisch demonstrated that honeybees communicate the location of a distant food source to other honeybees in the hive via the "waggle dance" (reviewed in von Frisch 1993). The underlying estimate of distance was later shown to be the result of a visual "odometer" that integrates the apparent speed of the visual scene during flight (Esch et al. 2001). Since then, many other behaviors have been shown to be dependent on visual estimates of speed (reviewed in Srinivasan and Zhang 2004). Among these behaviors is the *centering response*, in which a honeybee matches the apparent image speed on each eye to center its flight path through a tunnel lined with sinusoidal or square wave patterns on the left and right walls (Kirchner and Srinivasan 1989). The reliability of the waggle dance and the centering response as behavioral measures have revealed a number of interesting properties of the underlying neural mechanisms.

Studies of the centering response by Srinivasan et al. (1993) suggested that the speed of the visual scene is estimated by a small-field mechanism that is insensitive to the direction of visual motion. In these experiments, a small section of the tunnel walls was replaced on one side with a computer monitor displaying a moving grating pattern, and on the other side with a transparent cover to allow for the

measurement of the vertical flight path. Since the transparent section of the wall was left empty, honeybees trained to fly through this tunnel demonstrated a characteristic "movement avoidance" response away from the computer screen and toward the empty wall. The magnitude of the response was dependent on the speed of the moving pattern. The lateral component of this response could be modulated by motion in both the horizontal and vertical directions, suggesting that the mechanism responsible for the centering response was non-directional. The authors then presented a grating stimulus with interleaved rows moving in opposite directions such that the average speed of the entire pattern was zero. The magnitude of the movement avoidance response to this stimulus was equal to that of a single grating moving at the same speed, contrary to what one would expect from a wide-field, directionally selective mechanism, indicating an underlying small-field mechanism. Further work by Dacke and Srinivasan (2007) demonstrated that both the vertical and the horizontal speed of the visual image contribute to the distance estimates of honeybees during foraging flights, necessitating a sensor that can measure speed in multiple directions.

Additional studies have demonstrated that the estimate of speed is largely independent of both spatial frequency and contrast of the patterns lining the tunnel walls (Srinivasan et al. 1996; Si et al. 2003). Centering studies have demonstrated that honeybees will fly through the center of a tunnel despite four-fold differences between the walls in the spatial frequency of a square wave pattern and two-fold differences between sinusoidal patterns (Srinivasan et al. 1991). These conclusions are supported by studies of the visual odometer, which have shown that honeybees will judge similar travel distances despite four-fold differences in the spatial frequency of square wave (Srinivasan et al. 1996) or sinusoidal (Si et al. 2003) patterns lining the tunnel walls.

Despite all this detailed behavioral information, we still have a poor understanding of how the brain processes visual information to yield an estimate of speed. Part of the problem lies in the apparent mechanism by which biological systems extract motion information from the intensity fluctuations detected by the photoreceptors. There is a strong evidence that biological motion detectors function by correlating the time-delayed outputs of adjacent photoreceptors (reviewed in Borst and Egelhaaf 1989). The outputs of these detectors, while motion sensitive, are generally dependent on the spatial and temporal frequency of the stimulus. This means that the speed tuning of these models to a narrowband (sinusoidal) stimulus will be different at each spatial frequency, making it difficult to estimate speed based solely on their outputs.

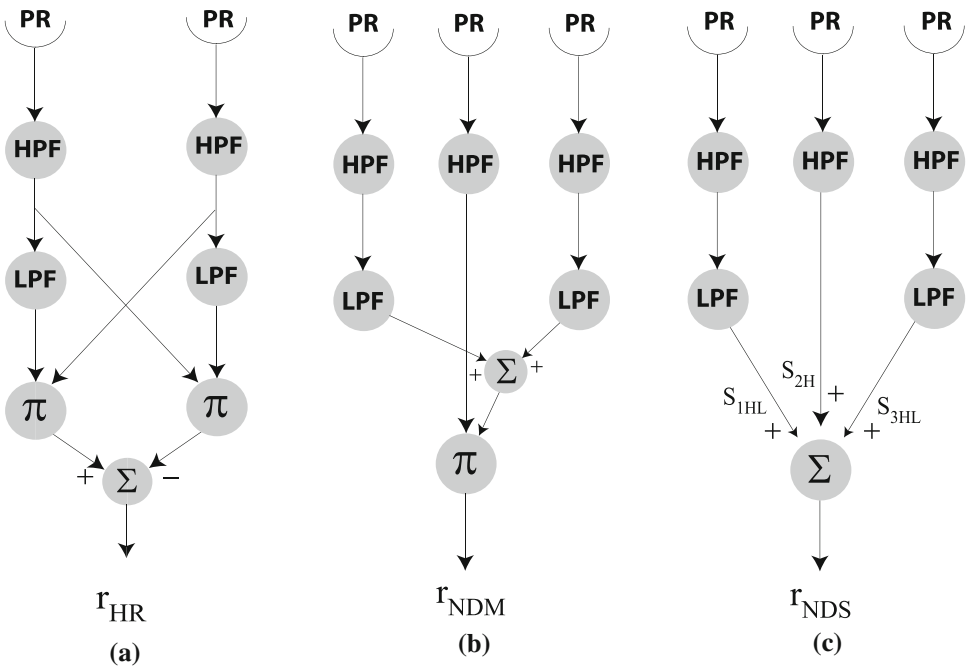

Fig. 1 Computational models of motion detection. Photoreceptor outputs (PR) are operated on by high-pass (HPF) and low-pass (LPF) filters. Different combinations of the filtered outputs can then be summed (Σ) and/or multiplied (π) to yield motion-sensitive outputs. **a** The Hassenstein–Reichardt (HR) model generates a directionally selective motion signal via the subtraction of two overlaid mirror-symmetrical subunits. Each subunit is composed of two spatially offset, high-pass filtered photoreceptor channels, one of which is also low-pass filtered. **b** The non-directional multiplication (NDM) model is composed of three spatially offset, high-pass filtered photoreceptor channels. In addition, the lateral channels are low-pass filtered and summed. The outputs of the central channel and the summed channels are then multiplied to yield a motion-sensitive output. **c** The non-directional summation (NDS) model is identical to the NDM model except the that final multiplication step is replaced by a summation. As a consequence, the NDS model is completely linear

Such is the case for the canonical model of motion detection in insects, the Hassenstein–Reichardt (HR) model (Fig. 1a; Hassenstein and Reichardt 1956; van Santen and Sperling 1985).

This conflict between modeling and behavior can be reconciled by analyzing the neuronal circuit that produces the HR-like outputs of cells in the insect brain. In the neuronally based model of the fly elementary motion detector (EMD) developed by Higgins et al. (2004), whose final output is comparable to that of the HR model, the authors noted that "non-directional motion" is computed prior to the final output of the putative dipteran EMD circuit. We define a non-directional motion detector as responding preferentially to motion over flicker but showing no preference for a direction of motion. One such non-directional motion detector was shown to have speed-tuned responses relatively independent of spatial frequency (Higgins 2004). This model, which we will refer to as the non-directional multiplication (NDM) model (Fig. 1b), exhibits a mean response proportional to the speed of an image and is relatively insensitive to the spatial frequency of a stimulus.

Further work by Rivera-Alvidrez (2005) investigating the EMD circuit yielded a more anatomically plausible non-directional model that we refer to as the non-directional summation (NDS) model (Fig. 1c). The NDS model is completely linear and has an *amplitude* response that is proportional to speed. Support for such non-directional models comes from anatomical studies of the early visual pathways of the fly, electrophysiological recordings from the Tm1 cell (Douglass and Strausfeld 1995), and modeling work on the EMD circuit (Higgins et al. 2004).

In order to reconcile the hypothesized physiological mechanisms of motion detection with the behavioral properties of visual speed estimation, we demonstrate how the NDS and NDM models can be used to mimic the real-world behaviors seen in honeybees using a relatively simple computational framework. Since it has not been previously presented in the literature, we also elaborate on the response properties of the NDS model.

2 Methods

All numerical calculations and simulations were carried out in the *Matlab* package (The Mathworks, Natick, MA). A one-dimensional time-varying sinusoidal input with contrast C, temporal frequency ω_t and spatial frequency ω_x was used for numerical evaluations of the models and can be written as

$$S(x,t) = \frac{1}{2} \cdot (1 + C \cdot \sin(\omega_x \cdot x + \omega_t \cdot t)) \tag{1}$$

Note that the speed of the sinusoidal stimulus, $v = \frac{\omega_t}{\omega_x}$, is dependent on both the temporal and spatial frequencies. To represent luminance, this sinusoid is offset such that it never reaches negative values.

A contrast-reversing sinusoid, used to investigate the flicker response of the NDS model, can be expressed as

$$S_C(x,t) = \frac{1}{2} \cdot (1 + C \cdot \sin(\omega_x \cdot x) \cdot \sin(\omega_f \cdot t)) \tag{2}$$

where ω_f is the temporal frequency of the contrast reversals.

The temporal filters used were all first-order linear filters with time constants of $\tau_1 = 2$ ms for the high-pass filters, matching the physiological data for high-pass filtering in the early visual pathways (Juusola et al. 1995), and $\tau_2 = 50$ ms for the low-pass filters matching the value used by Higgins (2004). The magnitude responses of the high-pass filters h_1 and low-pass filters h_2 can be expressed as

$$h_1(\omega_t) = \frac{\omega_t \cdot \tau_1}{\sqrt{1 + (\omega_t \cdot \tau_1)^2}} \tag{3}$$

$$h_2(\omega_t) = \frac{1}{\sqrt{1 + (\omega_t \cdot \tau_2)^2}} \tag{4}$$

The phase shift resulting from the application of the high-pass filters was identical for all pathways and can thus be ignored. In contrast, the selective application of the low-pass filter added a phase term ϕ_2 that can be expressed as

$$\phi_2(\omega_t) = -\tan^{-1}(\omega_t \cdot \tau) \tag{5}$$

With no loss of generality, the spacing between photoreceptors was set to one. The relative phase between sinusoidal inputs at neighboring photoreceptors was then $\phi_x = \omega_x$.

For the behavioral simulations, the eyes of the honeybee were composed of two semicircular arrays containing a total of 90 photoreceptors (Fig. 2). The visual field of the the bee, spanning 180°, was determined by calculating the visual projection of the world at a single point. This projection was synthesized at high resolution and then downsampled by a factor of 10 to smooth the sharp edges in the image that would otherwise create discontinuities in the motion detector responses. The visual field was then divided into pixels such that each photoreceptor (PR) had an angular spacing of approximately 2° in agreement with studies in honeybees (Seidl and Kaiser 1981). The outputs of the eight central photoreceptors were shared by both eyes in order to mimic the binocular overlap zone in both flies (Beersma et al. 1977) and bees (Seidl and Kaiser 1981). The PR outputs were processed by Motion Units (MU) with receptive fields either two (HR) or three (NDM and NDS) pixels wide. Sequential MUs were offset by a single pixel so that each eye contained either 48 (HR) or 47 (NDM and NDS) units. The angle of the head of the simulated bee was held fixed relative to the length of the tunnel such that the left and right eyes were always directly facing their respective walls. This prevented the rotation of the visual field while the simulated bee was turning and is in agreement with studies in flies showing that

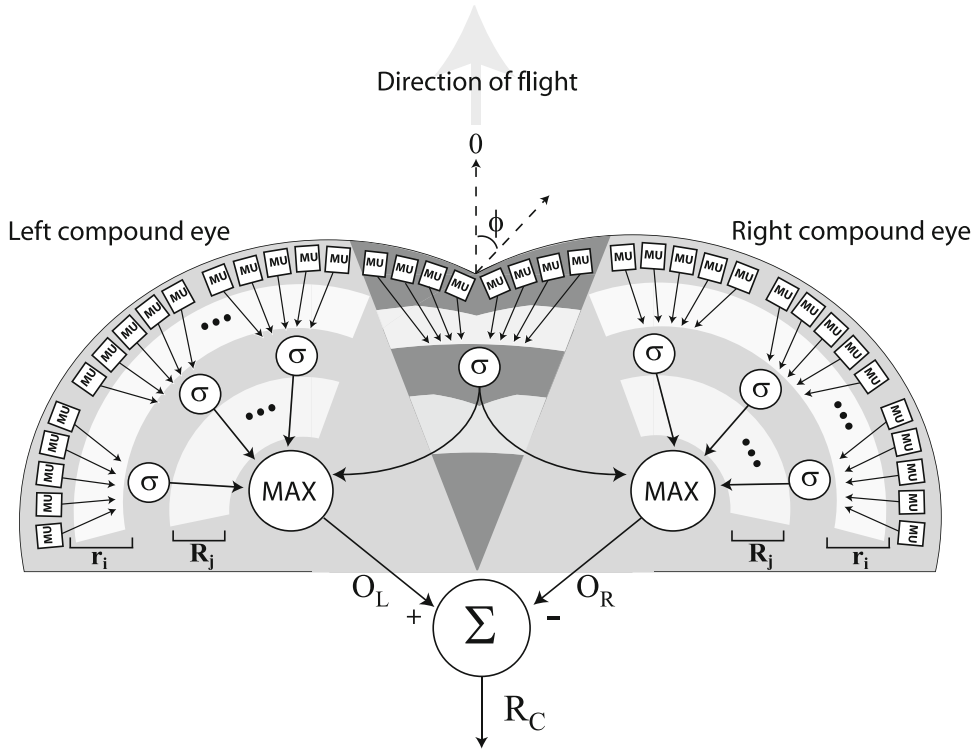

Fig. 2 Diagram of the behavioral simulation setup. The walls of the arena are denoted by the *dashed lines*. The eyes were composed of two slightly overlapping semicircular arrays of Motion Units (MU). The *shaded region* in the center delineates the binocular overlap zone, composed of eight overlapping photoreceptors. Each photoreceptor shared the same focal point, but had a different viewing angle (ϕ) defined relative to the forward direction ($\phi = 0$). As such, the head of the bee is dimensionless (a single point), but the eyes are split in the figure for diagrammatic purposes. Adjacent MUs were grouped into subfields and their outputs, r_i, were averaged (σ). The maximal response from the subfield outputs (R_j) of each eye were used as the global speed estimates for each eye (O_L and O_R). The final outputs from each eye were then subtracted (Σ) to yield a turn command (R_C)

head angle is held constant during translational flight (van Hateren and Schilstra 1999).

Our method for deriving a global estimate of speed for each eye, the reasoning for which will be detailed in Sect. 3, was as follows. MUs were first subdivided into five non-overlapping subfields, such that each subfield spanned approximately 18° (Srinivasan et al. 1993). With the exception of the two most central subfields, each contained nine adjacent MUs whose responses (r_i) were averaged (σ) to determine the subfield response (R_j). The maximal response from the subfield outputs of each eye were used as the global speed estimates for each eye (O_L and O_R). These outputs were subtracted to yield a turn command (R_C). The turn command was then multiplied by a gain scale factor (g) to specify an angular velocity ($\dot{\theta}$). The maximum magnitude of the angular velocity was limited to 45°/s; in addition to better mimicking gradual, real-world flight paths of honeybees, this limit also prevented the simulations from becoming unstable.

For a simulated bee traveling at fixed speed v_b, the x and y positions and angular orientation of the body θ at each time step t were specified by the equations:

$$\dot{\theta}(t) = g \cdot R_\mathrm{C}(t) \tag{6}$$

$$\theta(t) = \theta(t-1) + \dot{\theta}(t) \cdot \Delta t \tag{7}$$

$$x(t) = x(t-1) + v_b \cdot \cos\theta(t) \cdot \Delta t \tag{8}$$

$$y(t) = y(t-1) + v_b \cdot \sin\theta(t) \cdot \Delta t \tag{9}$$

The simulated bee navigated through an arena of length 400 cm and width 12 cm (Fig. 3) at speeds ranging from 30 to 50 cm/s to match real-world experimental conditions (Srinivasan et al. 1991). To avoid discontinuities at the beginning and end of the tunnel, simulation runs were limited to the middle 200 cm of the arena as denoted by the dashed black lines in Fig. 3. During the first 20 time steps, the angular velocity of the bee was held at zero in order to ignore startup transients from the temporal filters. Simulations were stopped when the bee traveled 200 cm along the length of the tunnel or upon contact with one of the walls.

Two different types of arenas were used for the behavioral simulation experiments. The first arena was composed of rows of objects that were projected into the visual field of the simulated bee. The size of the objects in the visual field varied inversely with their Euclidean distance from the bee (Fig. 4a), and in order to represent the visual angle, the objects would subtend on the retina as a function of distance. Spatial

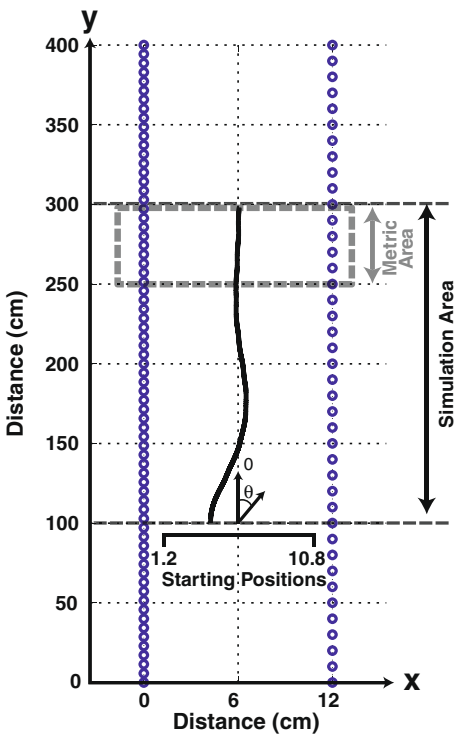

Fig. 3 Behavioral simulation arena. *Black circles* denote the 400 cm long tunnel walls that were composed of columns of equally spaced objects or the lateral distance of a grating pattern that was projected onto the eyes of the simulated bee. The width of the tunnel was 12 cm. The *dashed black lines* delineate the 200 cm long section of the arena in which simulations were run. The *dashed gray box* indicates the 50 cm length of the tunnel where the performance metric was calculated. The *labeled bracket* indicates the range of starting positions used for simulations runs. The angle θ represented the body angle of the simulated bee and was defined relative to the forward (vertical) flight direction where $\theta = 0$. The *solid black line* is an example path of a simulated bee and is included for illustration

frequency was varied by changing the number of objects on each wall.

To better test the narrowband spatial frequency dependence of the models in behavioral simulations, we used a second method to construct the visual field in which an infinitely long tunnel lined with periodic sinusoidal or square wave patterns with contrast $C = 1$ was projected onto each eye of the simulated bee (Fig. 4b, c) using the following equation arising from the geometry of the visual projection

$$I(\phi) = 1 + C \cdot f\left(2\pi \cdot \omega_x \cdot \left(y + \frac{(D+x)}{\tan(\phi)}\right)\right) \qquad (10)$$

where f denotes a sine or square wave function, ω_x denotes the spatial frequency of the grating, x was the lateral position of the bee in the tunnel (centimeters), y was the horizontal distance of the bee along the length of the tunnel also in centimeters, $D = 6$ cm was the half-width of the tunnel and ϕ was the viewing angle of the photoreceptor in radians relative to the forward direction. The same tunnel width

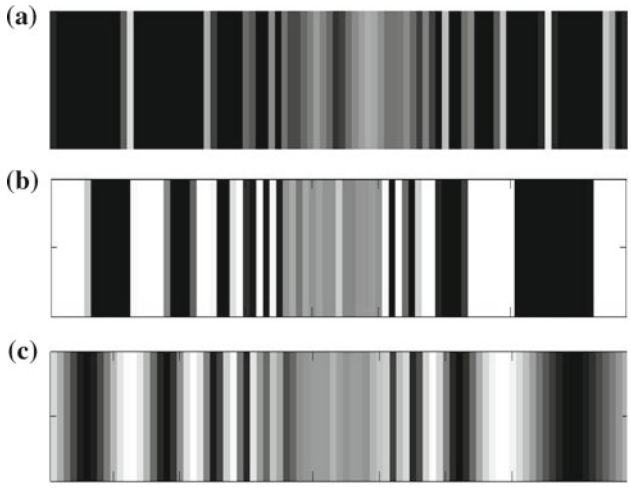

Fig. 4 Example visual fields. Examples of the three types of rendered visual fields used for behavioral simulations: **a** square wave grating using point objects, **b** true square wave grating (Eq. 10), and **c** sine wave grating (Eq. 10)

and state equations were used regardless of which method was used to construct the visual field of the simulated bee. The infinite length of the tunnel using this second method increased the activation of the frontal visual field and had the potential to create differences between the results of the two types of simulations. However, these differences were mitigated because of the very slow speed of image motion at these angles.

Multiple simulations with different starting positions and flight speeds (v_b) were performed for each experimental condition using identical parameter values for both arenas. The starting position along the lateral dimension of the tunnel varied between x positions of 1.2–10.8 cm and the flight speed v_b between 30–50 cm/s. Trials in which the bee passed through one of the walls were counted as failures. For each successful simulation run, the mean distance of the bee from the center of the arena ($\overline{x}$) along the final one quarter length of the tunnel (dashed gray box, Fig. 3) was used as a performance metric. This metric was chosen because it measured the average lateral position of the bee during steady-state flight, providing information about any biases in the path while ignoring initial transient maneuvering. To measure the overall performance of the bee for each experimental condition, we calculated the mean and standard deviation of $\overline{x}$ across successful trials.

3 Results

Speed responses of the three motion-sensitive models shown in Fig. 1, the HR, the NDM, and the NDS models, were tested and compared in theoretical and behavioral simulation frameworks.

3.1 Theoretical speed tuning

The version of the HR model used for our simulations is shown in Fig. 1a. The outputs of two spatially separated photoreceptors are first temporally high-pass filtered to removed sustained illumination components. Next, one of the outputs is low-pass filtered, adding a differential phase delay, and multiplied with the undelayed output. This operation is repeated in a mirror-symmetrical fashion after which the processed outputs are subtracted from each other to yield a directionally selective response. The time-averaged output of the HR model in response to a sinusoidal stimulus (Eq. 1), as derived in Higgins (2004), is

$$\bar{O}_{\mathrm{HR}} = \frac{C^2}{4} \cdot \frac{(\omega_t \cdot \tau_1)^2}{(1+(\omega_t \cdot \tau_1)^2)} \cdot \frac{(\omega_t \cdot \tau_2)}{(1+(\omega_t \cdot \tau_2)^2)} \cdot \sin(\omega_x) \tag{11}$$

Because of the ω_t^3 term in this expression, the sign of the HR response will change with the direction of motion. We were only interested in the speed estimate of the model so we used the absolute value of this mean response to represent the speed estimate of the model.

The mean responses of the HR model to sinusoidal gratings of different spatial frequencies moving at different speeds are plotted in Fig. 5a (top), where we have substituted in $\omega_t = v \cdot \omega_x$. The mean response of the HR model increases non-linearly with speed. The magnitude of the responses changes dramatically as the spatial frequency is varied. This dependence on spatial frequency can be seen more clearly in the contour plot (Fig. 5a, bottom) where vertical contour lines would indicate a speed tuning independent of spatial frequency. The lack of vertical lines in the plot demonstrate that the HR model is not speed-tuned in the range of image speed typically seen during flight.

Using the mean response of the HR model as a benchmark, we can compare the motion responses of the two non-directional models beginning with the NDM model (Fig. 1b). As derived by Higgins (2004), the time-averaged response of the NDM model to a sinusoidal input (Eq. 1) is

$$\bar{O}_{\mathrm{NDM}} = \frac{C^2}{4} \cdot \frac{(\omega_t \cdot \tau_1)^2}{(1+(\omega_t \cdot \tau_1)^2) \cdot (1+(\omega_t \cdot \tau_2)^2)} \cdot \cos(\omega_x) \tag{12}$$

A plot of NDM model mean responses to sinusoids of different spatial frequencies moving at different speeds is shown in Fig. 5b (top). Unlike the HR model, the response of the NDM model increases approximately linearly with speed and shows much less spatial frequency dependence. The contour plot (Fig. 5b, bottom) provides a better visualization of how this proportional response to speed changes with spatial frequency. Compared to the HR model, the NDM model is speed-tuned at a broader range of speeds and at lower spatial frequencies.

An alternative non-directional model, the NDS model, was proposed by Rivera-Alvidrez (2005) after working on a neuronally based model of elementary motion detection (Higgins et al. 2004). The NDS and NDM models differ only in the final step: the final multiplication of the NDM model is replaced by a summation (Fig. 1). The ramifications of the change are dramatic, both in terms of the ease of neuronal implementation and in the response properties of the model.

To show this, we begin with the same sinusoidal stimulus (Eq. 1) used for the previous derivations. The overall model response is simply the sum of the filtered photoreceptor outputs marked $S_{1\mathrm{HL}}$, $S_{2\mathrm{H}}$ and $S_{3\mathrm{HL}}$ in Fig. 1c. Assuming, without loss of generality, that the absolute phase difference between the stimulus and the left-most photoreceptor is zero, the filtered outputs can be written as follows:

$$S_{1\mathrm{HL}} = \frac{C}{2} \cdot h_1 \cdot h_2 \cdot \sin(\omega_t \cdot \tau + \phi_2) \tag{13}$$

$$S_{2\mathrm{H}} = \frac{C}{2} \cdot h_1 \cdot \sin(\omega_t \cdot \tau + \phi_x) \tag{14}$$

$$S_{3\mathrm{HL}} = \frac{C}{2} \cdot h_1 \cdot h_2 \cdot \sin(\omega_t \cdot \tau + \phi_2 + 2 \cdot \phi_x) \tag{15}$$

The amplitude response for the NDS model can then be expressed as

$$A_{\mathrm{NDS}} = \frac{C}{2} \cdot h_1 \cdot \sqrt{4 \cdot h_2 \cdot ((h_2 \cdot \cos^2(\omega_x) + \cos(\omega_x) + \cos(\phi_2)) + 1} \tag{16}$$

Substituting in Eqs. 3, 4, and 5 then yields the equation:

$$A_{\mathrm{NDS}} = \frac{C}{2} \cdot \frac{\omega_t \cdot \tau_1}{\sqrt{1+(\omega_t \cdot \tau_1)} \cdot \sqrt{1+(\omega_t \cdot \tau_2)}} \cdot \sqrt{[2 \cdot \cos(\omega_x) + 1]^2 + (\omega_t \cdot \tau)^2} \tag{17}$$

Note that this is the amplitude, as opposed to the mean, response of the model. Since it is linear, the mean response of the NDS model over one cycle of a sinusoid is equal to zero. The amplitude response of the NDS model increases proportionally to speed much like the mean response of the NDM model (Fig. 5c). Combined with the weak spatial frequency tuning of the model at lower speeds (Fig. 5c, bottom), the NDS model can be used as a very effective speed estimator.

The NDS model also responds more strongly to motion than to flicker. Using Eq. 2 (counter phase flicker) as input, the response of the NDS model can be shown to be

$$A_{\mathrm{NDS_{CF}}} = \frac{C}{2} \cdot h_1 \cdot \sin(\omega_x \cdot (p_0 + 1)) \cdot \sqrt{4 \cdot h_2 \cdot [(h_2 \cdot \cos^2(\omega_x) + \cos(\omega_x) + \cos(\phi_2)] + 1} \tag{18}$$

where p_0 indicates the angular position, in degrees, of the leftmost photoreceptor relative to a sinusoidal grating fixed in space. This is identical to Eq. 16 except for the additional

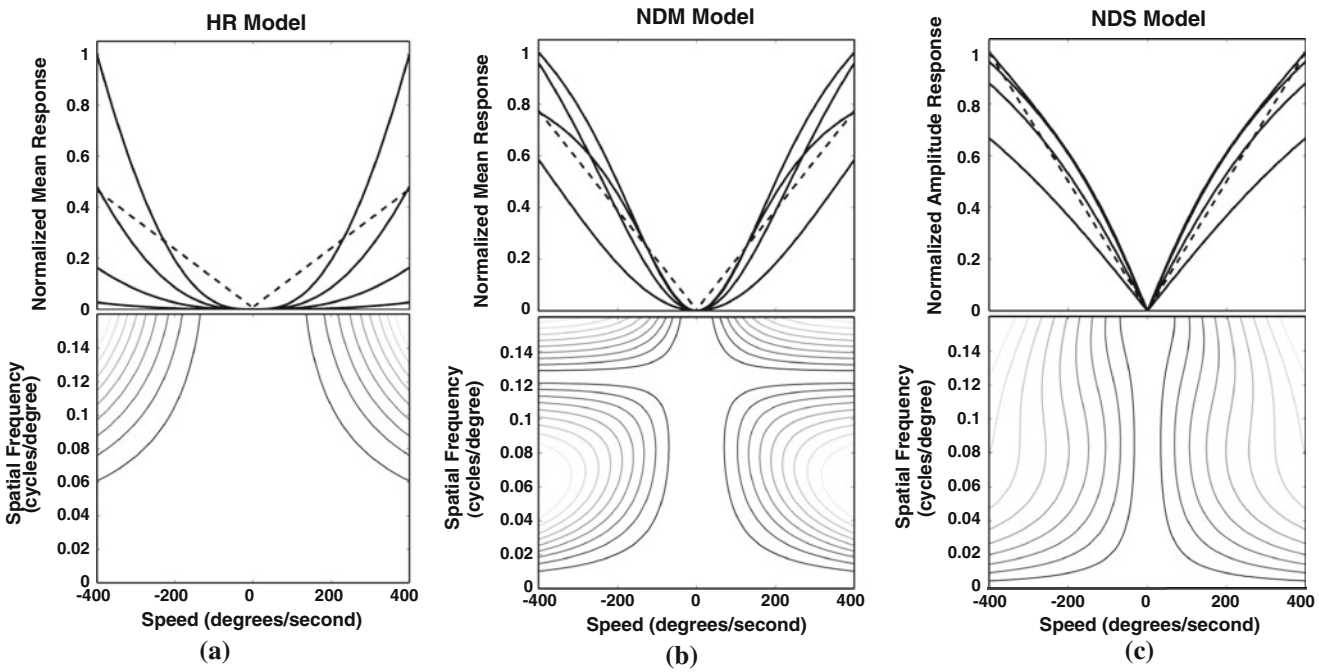

Fig. 5 Model speed tunings, where $\omega_t = v \cdot \omega_x$ has been substituted into Eqs. 11, 12, and 17. **a** *Top*: The normalized, rectified response of the HR model (Eq. 11). *Solid lines* indicate model responses to sinusoidal gratings of 0.03 (minimum peak response), 0.05, 0.07, and 0.09 (maximum peak response) cycles per degree. Centering experiments in honeybees have used sinusoidal gratings with frequencies of 0.017, 0.038, and 0.07 cycles/degree and square wave gratings ranging from 0.01 to 0.04 cycles/degree. The *dashed line* is representative of a linear speed response. *Bottom*: Contour plot demonstrating the variation of the rectified HR model response relative to speed and spatial frequency. *Darker lines* represent weaker model responses. *Vertical lines* would indicate spatial frequency independent response to speed. **b** *Top*: Normalized response of the NDM model (Eq. 12) plotted against speed. *Solid lines* denote responses at spatial frequencies of 0.07 (maximum peak response), 0.05, 0.09, and 0.03 (minimum peak response) cycles per degree. Note the reversal of maximal and minimal peak responses relative to the rectified HR model. *Bottom*: Contour plot of NDM model response relative to speed and spatial frequency. **c** *Top*: Normalized and rectified NDS model amplitude response (Eq. 17) plotted against speed. *Solid lines* denote responses at spatial frequencies of 0.03 (minimum peak response), 0.05, 0.07, and 0.09 (maximum peak response) cycles per degree. *Bottom*: Contour plot of NDS model response relative to speed and spatial frequency

$\sin(\omega_x \cdot (p_0+1))$ term that has a maximum value of one. Thus, the average response to flicker is less than that to motion, but the responses can be equal depending on the spatial position of the grating.

3.2 Behavioral simulations

Next, we wanted to test the extent to which the theoretical differences between the models would be reflected in a behavioral setting. To this end, we implemented all three models in a behavioral simulation framework (Fig. 2) and compared their efficacy for mimicking centering behaviors.

As derived previously, the raw outputs from the individual models are not themselves speed-tuned, but rather are speed dependent in either their mean or amplitude responses. Rather than taking an explicit temporal mean of model outputs, we approximate a temporal mean by averaging spatially (discussed further below). Since we use the absolute mean response of the HR model to represent its speed estimate, we take the absolute value of the spatially averaged HR outputs. The NDM model, which represents speed in its mean response with a strictly positive signal, requires only spatial averaging. To extract a speed estimate from the NDS model, which represents speed in its *amplitude*, we took the absolute value of individual NDS model outputs prior to spatial averaging. Since the temporal mean of a rectified sinusoid with amplitude A is $\frac{2 \cdot A}{\pi}$, this makes the signal linearly proportional to the amplitude of NDS outputs, and thus proportional to speed.

A key component of the behavioral simulation setup was acquiring a global estimate of speed from the arrays of small-field MUs making up each eye. We tested a number of different methods for spatial collation of the individual model responses including: straight and weighted averages of the model responses; taking the maximal response from each eye; taking a weighted average of the maximal responses from each eye; and finally, taking the maximum subfield response as described in the Methods section.

The maximal subfield collation proved advantageous for a number of reasons. First, the straight and weighted averaging functions consistently failed because they were inherently dependent on the overall illumination; whichever wall

had more objects naturally provided a stronger average signal. On the other hand, methods using the maximal MU response from each eye had dramatic fluctuations in value at each time step. The fluctuation in the responses between the eyes resulted in very jittery, oscillatory paths unless the gain scale factor was set extremely low. However, lowering the gain scale factor hampered the ability of the simulated bee to respond to high speeds and increased the number of failed simulation runs. Taking a weighted average of the maximal responses addressed this problem, but did not improve the performance beyond that of the maximal subfield method.

A major advantage of the maximal subfield method was that it approximated a temporal average. If the same periodic stimulus is seen by all the MUs, then a spatial average approximates a temporal average as long as multiple periods are present within a fixed subfield. Assuming a constant speed, the approximation holds for high spatial frequencies (below the Nyquist limit) relative to the subfield size, with the approximation being exact only for infinite eye spatial resolution. As the spatial frequency of a sinusoid increases, a larger number of cycles will be averaged within each visual subfield, giving a more accurate estimate of the temporal mean response. As the spatial frequency decreases, the spatial period will eventually exceed the size of the subfield, giving a partial average. In our simulations, each subfield covered approximately 18° so that this only became a problem when the bee was extremely close to a wall, thereby greatly decreasing the apparent spatial frequency of the wall. However, one faces a similar challenge in using a temporal average. As the spatial frequency decreases, one needs to average over a longer period of time in order to get an accurate estimate of the mean response. While spatially averaging the MU responses was an imperfect approximation of the temporal mean response, it was generally accurate and had the advantage of giving an instantaneous estimate of speed.

We were most interested in testing the spatial frequency dependence of the different models in centering simulations. Behavioral experiments have shown that bees are capable of visually estimating speed despite four-fold differences in the spatial frequency of square wave grating patterns (Srinivasan et al. 1991). Our first set of simulation experiments used evenly spaced point objects to approximate square wave gratings. The number of objects on one wall was varied such that the approximate spatial frequencies ranged from 0.1 to 0.4 cycles/cm. The spatial frequency of the opposite wall was held constant at either 0.2 or 0.1 cycles/cm. Multiple trials at different speeds and starting positions were run for each set of spatial frequencies and the results are presented in Fig. 6a.

As can be seen, all of the models showed some dependence on spatial frequency by tending toward the lower spatial frequency wall. This dependence was small when the spatial frequency of one wall was held constant at 0.2 cycles/cm, with the largest deviation being 1.5 cm from the center of the tunnel. The simulated bee displayed significantly larger deviations from the center of the tunnel when a constant spatial frequency of 0.1 cycles/cm was used. However, even in this case the bee did not range more than 2.5 cm from the center of the tunnel. On average the HR model displayed the least dependence on spatial frequency while the NDM model outperformed the other two models when the average spatial frequency was high. The NDS model was the most dependent on spatial frequency, the opposite of what one would have predicted based on the analytically derived responses. None of the results changed significantly with flight speed.

Because of these unexpected results we modified our simulations so that we could present true sine or square wave stimuli. Using this second method, we performed the same set of experiments with true square wave gratings (Fig. 6b). The most notable difference is the inversion of the path bias for the NDM model. While in the previous simulations the NDM model caused the bee to fly closer to the low frequency wall, the bee instead approached the higher frequency wall. In addition, the NDM model deviated further from the center of the tunnel, especially at high spatial frequencies. While the polarity of the HR and NDS model responses remained the same the relative efficacy of the two models was reversed, with the NDS performing better than the HR model. All of the models showed significantly less variability between trials when true square wave gratings were used.

When sinusoidal patterns were used to line the tunnel walls (Fig. 6c), there were again dramatic changes in model performance. The HR model proved incapable of successfully navigating the tunnel except when the spatial frequencies of the sinusoidal gratings were the same, and even then only when the simulations were started from the center of the tunnel (data not shown). In contrast, the non-directional models successfully navigated the length of the tunnel, although they showed larger deviations from the center than observed previously. The direction of the NDM model response reverted to that observed when point objects were used, with the simulated bee approaching the lower frequency wall. When the NDS model was used, the lateral position of the bee changed approximately linearly with spatial frequency and the variation across trials was much larger than with square wave gratings. These results qualitatively match with those of Srinivasan et al. (1991) who found that the lateral flight paths of honeybees are more sensitive to narrowband stimuli, such that they are biased by two-fold differences in the spatial frequency of sinusoidal patterns versus four-fold differences between square wave gratings.

Our second set of simulation experiments tested the efficacy of each model for accurately measuring the speed of a moving wall. These experiments were based on those of

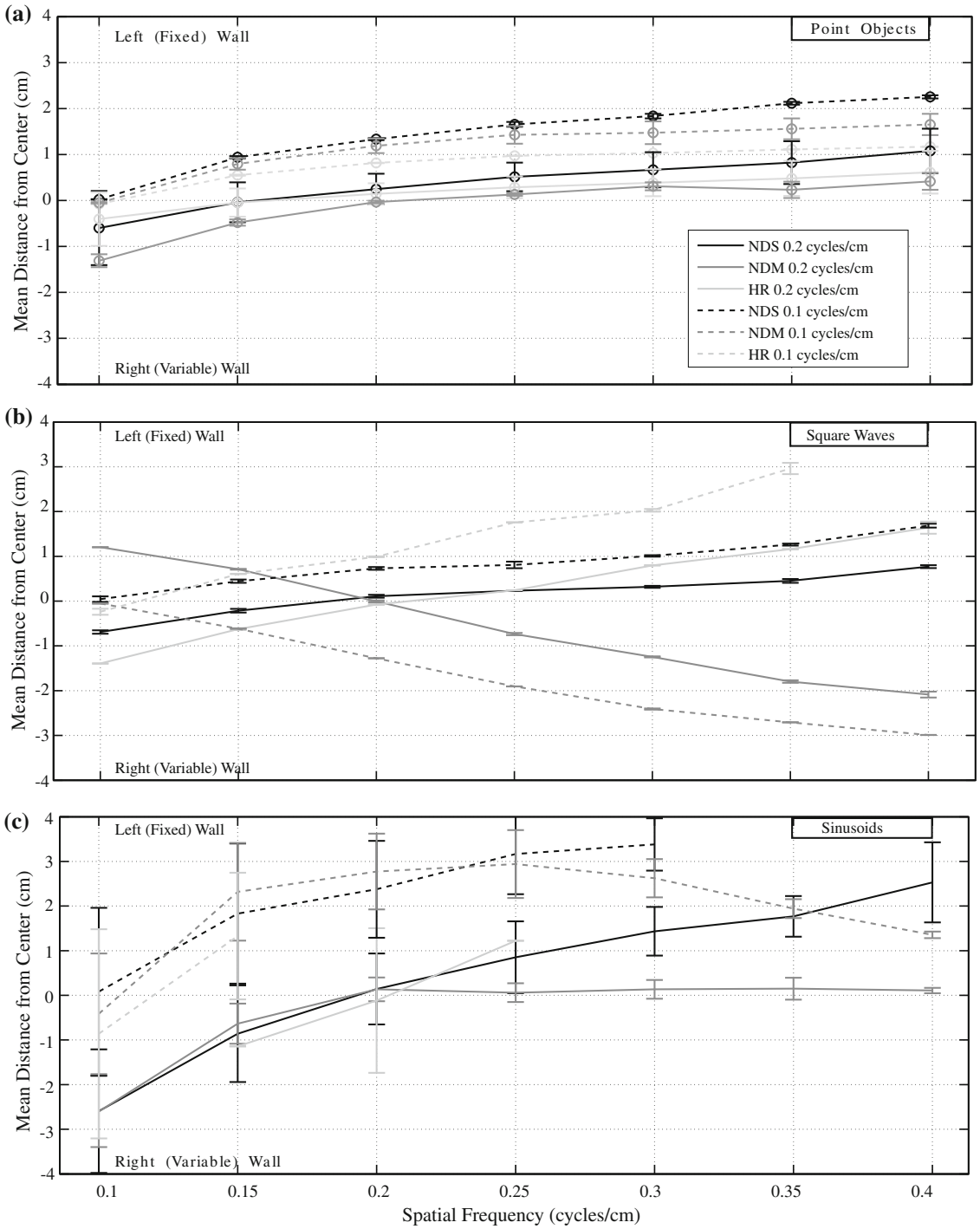

Fig. 6 The effect of spatial frequency on model performance. The mean lateral position of the bee along the last quarter of the tunnel is plotted versus the spatial frequency of the right (variable) wall while the spatial frequency of the left (fixed) wall was held constant at either 0.1 cycles/cm (*dashed lines*) or 0.2 cycles/cm (*solid lines*). The results are shown for three different types of stimuli: **a** evenly spaced point objects, **b** square wave gratings, and **c** sinusoidal gratings. The mean and standard deviation of the mean positions of the bee for each trial were calculated and are plotted for the HR (*light gray*), NDM (*dark gray*), and NDS (*black*) models. For each condition, the starting position and speed of the bee were varied across trials

Srinivasan et al. (1991) in which the lateral position of the honeybees' flight path through a tunnel was biased by moving one of the tunnel walls. Moving the wall in the direction of flight (positive wall speed) reduced the apparent speed of the wall, and resulted in the honeybee flying closer to the moving wall. The opposite was also true; moving one wall

opposite the direction of flight (negative) caused the bee to fly further from that wall.

In our moving wall simulation experiments, the spatial frequency of each wall was held constant at 0.2 cycles/cm and the speed of the left wall was varied between −30 and 30 cm/s. The change in the mean lateral positions as a function of wall speed is plotted for a simulated bee flying at 40 cm/s using the three different types of gratings (Fig. 7). These results are compared to the expected distance from the center d_c (in cm) of a bee perfectly balancing the apparent image motion on each eye, adapted from Srinivasan et al. (1991), which can be expressed as

$$d_c = 120 \cdot \frac{1 - v_r}{2 - v_r} - 60 \tag{19}$$

where v_r is the ratio of the speed of the left wall to the speed of the bee.

When point objects were used for the visual stimulus (Fig. 7a) all three models fit the general shape of the scaled prediction. The HR and NDM models did not fully compensate for the changes in the apparent speed of the walls, while the NDS model displayed a much better match to the theoretical prediction.

Replacing the rows of objects with true square wave gratings (Fig. 7b) improved the performance of both the HR and NDS models. The NDM model once again responded very differently to true square wave grating stimuli and failed to compensate for the moving wall at speeds below 10 cm/s. Even at higher wall speeds, the NDM model still showed much smaller deviations than would be predicted by an ideal speed estimator.

Switching to narrowband gratings (Fig. 7c) greatly improved the NDM model performance and greatly diminished the effectiveness of the HR model. This was in agreement with our previous narrowband experiments, in which the HR model consistently failed to navigate the tunnel when sinusoids of different spatial frequency lined the walls of the tunnel. The NDS model performance also decreased, with the mean lateral position deviating from the ideal fit at negative wall speeds approximately linearly as the wall speed decreased below zero.

4 Discussion

In the present study, we compared the speed tunings of three models of motion detection: the HR, NDM, and NDS models. We developed a simulation framework to acquire small-field, non-directional estimates of the apparent image speed during flight, in accordance with behavioral experiments in honeybees. In particular, we were interested in the efficacy of the two non-directional models and benchmarked their performance versus that of the HR model. Our results suggest that while all three models can partially mimic speed-dependent behaviors given specific visual stimuli, only the NDS model was sufficiently robust to match the behaviors observed in honeybees over a range of conditions.

Surprisingly, the analytically derived model responses were not entirely predictive of our behavioral simulation results. While the NDS model was on average the most effective of the three models for mimicking centering behaviors independent of spatial frequency, it was outperformed by the NDM model when narrowband patterns were used in the behavioral simulations. Furthermore, the fact that the HR model could be used for mimicking centering behaviors when square wave gratings were used was contrary to what we expected based on the derived model responses (Fig. 6).

One possible explanation for the success of the HR model is that the higher spatial frequency harmonics present in the spectrum of the square wave gratings dominated the model response. The relatively large contribution of the high spatial frequency components compared to the lower spatial frequency components can be visualized with the help of Fig. 5a, in which the HR outputs at speeds below 200 degrees/second and spatial frequencies below 0.06 cycles/degree are so small that they are not even present in the contour plot. This suggests that even moderately high spatial frequency inputs will have much larger contributions to the overall HR model response. This hypothesis is consistent with previous observations that the HR model has speed-tuned responses to images with broad spatial frequency compositions, such as natural scenes (Dror et al. 2001).

Similarly, changes in the NDM model response at higher spatial frequencies may also help to explain some of the perplexing behavioral simulation results. The NDM model was more robust than the HR model, but showed a very strong dependence on spatial frequency when true square wave gratings were used. The multiplication operation present in the NDM model will magnify the model responses to higher spatial frequencies, increasing the relative contributions of the high spatial frequency harmonics of the square wave gratings. As can be seen in Fig. 5b, the response of the NDM model contains a notable trough at 0.13 cycles/degree and subsequently increases with increasing spatial frequency. This complicated response profile, with certain higher spatial frequencies having large contributions to the overall model response, is likely responsible for the perplexing behavior of the model to different grating stimuli.

For all three models, the largest deviations from the center of the tunnel occurred when the lowest spatial frequency tested (0.1 cycles/cm) was compared to a higher spatial frequency pattern. Two reasons for this deviation are the smaller number of edges, hence fewer motion cues, provided by the lower frequency wall and the decrease in the model responses

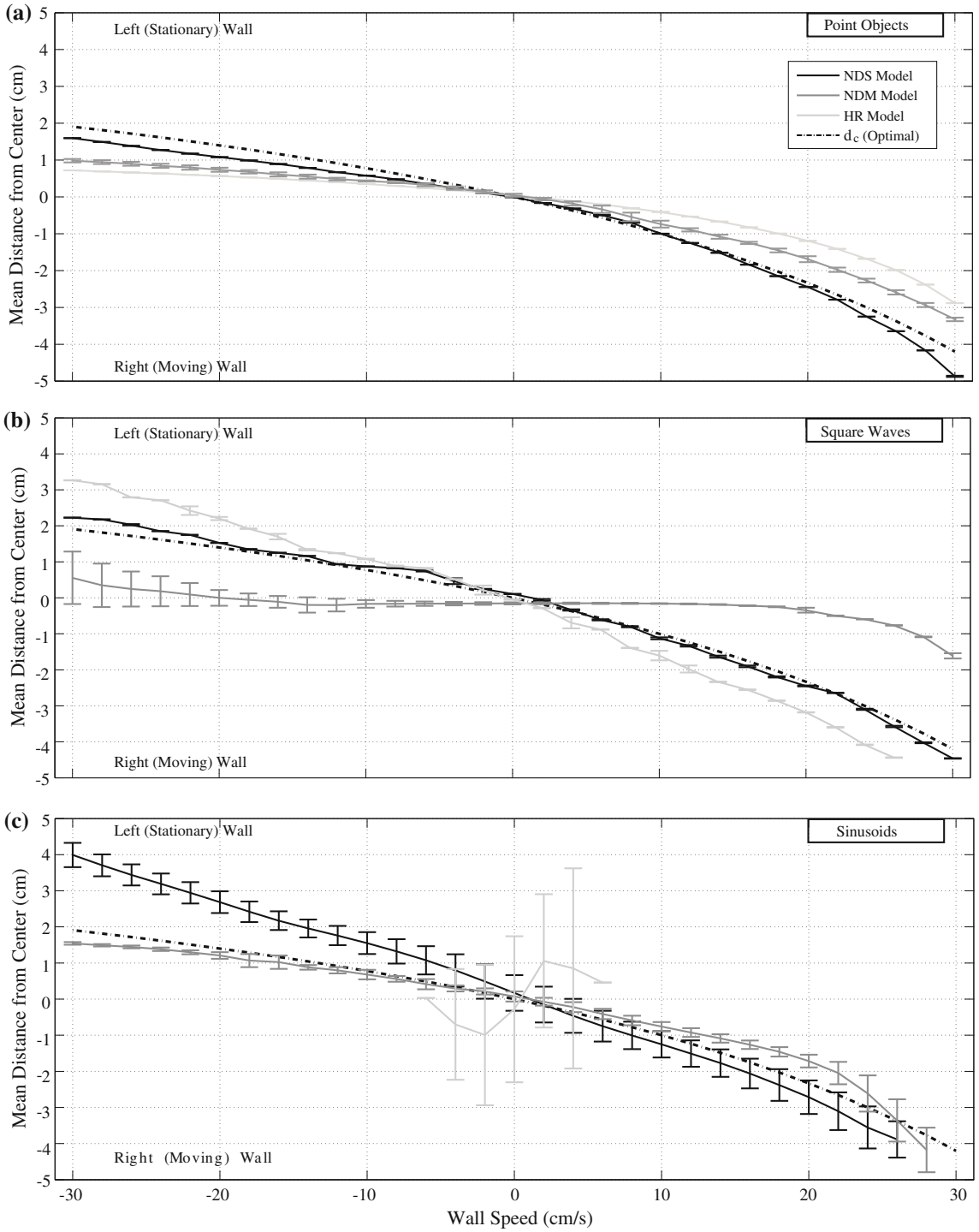

Fig. 7 The effect of moving one of the walls on centering simulations. The mean distance from the center of the tunnel for a simulated bee flying at 40 cm/s is plotted versus the speed of the left wall for the HR (*light gray*), NDM (*dark gray*), and NDS (*black*) models. The spatial frequency of the **a** point objects, **b** square wave gratings, or **c** sinusoidal gratings was the same for both walls (0.2 cycles/cm). The *black dashed line* is the predicted position of a bee perfectly matching the apparent speed of the walls d_c (Eq. 19). Each point represents the mean paths for trials run at starting positions between of −5.6 to 5.6 cm. Negative speeds indicate the right wall moving opposite the direction of flight and negative mean values indicate proximity to the right (moving) wall

at low spatial frequencies. These problems are unlikely to be experienced by a honeybee in a real-world environment where the bee would have wider horizontal ($|\phi| > 90°$) and vertical fields of view with other potential motion cues. Furthermore, honeybees may not perceive very low frequency gratings as periodic patterns.

In contrast to the spatial frequency variation experiments, the moving wall simulations better matched the predictions of the analytically derived model responses. The NDS model closely matched the predicted position of a bee perfectly matching the apparent speed of the walls (d_c, Eq. 19) and previous behavioral experiments (Srinivasan et al. 1991) for both square wave stimuli. In the case of narrowband patterns, the NDS model matched the shape of the ideal curve, but tended to overestimate the speed of the moving wall. Unfortunately, we lack any behavioral data from moving wall centering experiments using narrowband patterns so we cannot directly compare these simulation results with actual behavioral data. Simulations using the NDM and HR models using rows of objects matched the general shape of the curve, but the models were less effective when true square wave (NDM) or sinusoidal gratings (HR) were used.

The dependence of the ND models on spatial frequency, and the differential responses to square and sinusoidal gratings, are qualitatively consistent with experimental observations. Recent studies of the centering response in bumblebees have shown that the behavior is weakly dependent on the spatial frequency of sinusoidal stimuli outside of previously measured ranges (Dyhr and Higgins 2010). These results are consistent with the weak narrowband spatial frequency dependence of the honeybee centering response (Srinivasan et al. 1991). Furthermore, Dyhr and Higgins (2010) also observed small, but significant, differences in the centering response when comparing sinusoidal and square wave gratings of the same spatial frequency.

In our simulation setup, the head of the bee was always facing forward in order to eliminate rotational motion artifacts. This condition is consistent with observations in flies suggesting that the head remains fixed during forward flight and is quickly rotated when the insect is turning (van Hateren and Schilstra 1999). Our initial experiments included head rotation, but the additional motion caused a number of difficulties. The rotational motion signal would often outweigh that of translational motion, greatly altering the motion differential between the eyes. In addition, turning the head of the bee caused asymmetries in the relative input to each eye, often resulting in a failed simulations. Finally, in initial trials in which the directionality of the HR model was preserved, rotational motion often caused one of the eyes to produce a negative speed output, creating a positive feedback loop in which the simulated bee would continue to turn further in the same direction resulting in a failed simulation run.

For this study, we developed a novel method for using small-field motion to guide global behavior. Our solution to this problem was to average responses from small collections of cells and then select the largest response among these subfields. Although there is no specific biological evidence supporting such a mechanism, it could be implemented by a biological system using a network of cells that receive inputs from neighboring speed-sensitive cells. The collator cell with the largest response could then inhibit the neighboring cells, thereby implementing a winner-take-all function among these neurons.

While the HR model was surprisingly effective for mimicking optic flow dependent behaviors in our simulations, it is important to note that this required a number of additional processing steps. Many of these steps are inconsistent with the properties of HR-like computations performed by biological systems. Much of the biological support for the HR model comes from recordings of the wide-field, directionally selective lobula plate tangential cells of the fly (reviewed in Borst and Egelhaaf 1989). The responses of these cells peak at temporal frequencies between 30 and 40 Hz and almost completely disappear at 100 Hz. In contrast, optic flow dependent behaviors necessitate the detection of temporal frequencies at or above 100 Hz (Srinivasan et al. 1999). While our results suggest that the HR model can be used to explain some speed-dependent behaviors, the outputs of the lobula plate tangential cells cannot. Instead, this would require a separate pathway that is small-field, eliminates directional motion information and sensitive to high temporal frequencies. This would require significant additional processing and eliminates the main argument for the relevance of the HR model. It also begs the question of why the brain would compute the direction of motion only to later discard that information.

A parallel non-directional pathway for visual speed estimation provides a much simpler explanation for the biological basis of visual speed estimation. Optic flow dependent behaviors have been shown to be small-field, non-directional, and sensitive to flicker: all properties matched by the non-directional models. Non-directionally sensitive cells have been electrophysiologically identified in the early visual pathways of the fly (Douglass and Strausfeld 1995), the most notable being the Tm1 cell, and appear to precede the computation of directional motion (Higgins et al. 2004). Modeling work on the EMD in the fly suggest that the computation performed by the Tm1 cell is identical to that of the NDS model presented in this paper. Additional processing of the Tm1 cell output, in parallel to the directional motion computation, could easily extract optic flow information with minimal additional processing. More detailed electrophysiological recordings from these non-directional cells could shed further light onto this problem.

Alternative models have been proposed to explain optic flow behaviors, the most notable being the gradient-based scheme of Srinivasan et al. (1991), the Angular Speed Detector (ASD) of Riabinina and Philippides (2009) and the "token-matching scheme" used by Serres et al. (2008). One major disadvantage of these models is that the motion detection stages require sharp edges in order to function, necessitating a preprocessing step in which the visual image is

converted to a binary image via a thresholding operation before the models can be used as optic flow sensors (Srinivasan et al. 1991; Riabinina and Philippides 2009). While such a mechanism has been proposed for fly lamina monopolar cells (Srinivasan et al. 1991), none of these models have biological plausibility comparable to correlation-type schemes.

One component necessary to achieve the full range of optic flow dependent behaviors is a speed control mechanism. Other studies have specifically investigated potential control systems for using optic flow for centering and flight speed control, but have used very basic speed detectors (Serres et al. 2008). Our study was focused on the biological mechanism underlying visual speed estimation, but adding a more sophisticated navigational algorithm to our simulations may improve our results and subsequent predictions. However, the qualitative performance of the models is unlikely to change.

While both the non-directional models displayed some dependence on spatial frequency in our behavioral experiments, it may be possible to alter the models in order to broaden their spatial frequency tuning. The effectiveness of all of the models was heavily dependent on the filter time constants (data not shown). Unlike other modeling studies (Higgins et al. 2004; Higgins 2004; Riabinina and Philippides 2009), we used a much smaller high-pass filter time constant of $\tau_1 = 2$ ms to match the apparent high-pass filtering between the photoreceptor-L2 synapse (Juusola et al. 1995). Increasing the time constant up to 50 ms significantly reduces the range of speeds that the models can respond to, suggesting that it may be possible to modify the time constants to optimize the speed tuning of the models. Even a slight shift in the spatial frequency tuning of the NDS model toward lower frequencies will likely to improve the effectiveness of the model for mimicking centering behaviors.

Among the three models considered in this study, the NDS model is the one that best describes the centering response behavior that is actually observed in insects. The NDS model is also non-directional, consistent with the behaviorally measured centering response (Srinivasan et al. 1993). Therefore, among all the extant models in the literature, the NDS model appears to best describe the movement-detecting system that underlies the centering response.

Acknowledgments This work was supported by individual fellowships from the NSF IGERT program and the BIO5 institute awarded by the Biology, Math and Physics Initiative at the University of Arizona. Support was also provided by the NIH through an NINDS NRSA pre-doctoral fellowship (1F31NS053433) and by the NCRR (Grant No. 5R01RR008688-21). The authors would also like to thank the reviewers for their helpful comments and suggestions for improving the manuscript.

References

Beersma D, Stavenga D, Kuiper JW (1977) Retinal lattice, visual field and binocularities in flies. J Comp Physiol A 119:207–220

Borst A, Egelhaaf M (1989) Principles of visual motion detection. Trends Neurosci 12(8):297–306

Dacke M, Srinivasan M (2007) Honeybee navigation: distance estimation in the third dimension. J Exp Biol 210(5):845–853

Douglass J, Strausfeld N (1995) Visual motion detection circuits in flies: peripheral motion computation by identified small-field retinotopic neurons. J Neurosci 15(8):5596–5611

Dror R, O'Carroll D, Laughlin S (2001) Accuracy of velocity estimation by Reichardt correlators. J Opt Soc Am A 18(2): 241–252

Dyhr JP, Higgins CM (2010) The spatial frequency tuning of optic-flow-dependent behaviors in the bumblebee *Bombus impatiens*. J Exp Biol 213:1643–1650

Esch H, Zhang S, Srinivasan M, Tautz J (2001) Honeybee dances communicate distances measured by optic flow. Nature 411(6837): 581–583

Hassenstein B, Reichardt W (1956) Systemtheoretische Analyse der Zeit-, Reihenfolgen- und Vorzeichenauswertung bei der Bewegungsperzeption des Rüsselkäfers Chlorophanus. Z Nat B 11(9): 513–524

Higgins C (2004) Non-directional motion may underlie insect behavioral dependence on image speed. Biol Cybern 91(5): 326–332

Higgins C, Douglass J, Strausfeld N (2004) The computational basis of an identified neuronal circuit for elementary motion detection in dipterous insects. Vis Neurosci 21(04):567–586

Juusola M, Weckstrom M, Uusitalo R, Korenberg M, French A (1995) Nonlinear models of the first synapse in the light-adapted fly retina. J Neurophysiol 74(6):2538–2547

Kirchner W, Srinivasan M (1989) Freely flying honeybees use image motion to estimate object distance. Naturwissenschaften 76(6): 281–282

Riabinina O, Philippides A (2009) A model of visual detection of angular speed for bees. J Theor Biol 257(1):61–72

Rivera-Alvidrez Z (2005) Computational modeling of neurons involved in fly motion detection. Master's thesis, University of Arizona, Tucson, Arizona

Seidl R, Kaiser W (1981) Visual field size, binocular domain and the ommatidial array of the compound eyes in worker honey bees. J Comp Physiol A 143(1):17–26

Serres J, Masson G, Ruffier F, Franceschini N (2008) A bee in the corridor: centering and wall-following. Naturwissenschaften 95(12):1181–1187

Si A, Srinivasan M, Zhang S (2003) Honeybee navigation: properties of the visually driven 'odometer'. J Exp Biol 206(8): 1265–1273

Srinivasan M, Zhang S (2004) Visual motor computations in insects. Annu Rev Neurosci 27:679–696

Srinivasan M, Lehrer M, Kirchner W, Zhang S (1991) Range perception through apparent image speed in freely flying honeybees. Vis Neurosci 6(5):519–535

Srinivasan M, Zhang S, Chandrashekara K (1993) Evidence for two distinct movement-detecting mechanisms in insect vision. Naturwissenschaften 80:38–41

Srinivasan M, Zhang S, Lehrer M, Collett T (1996) Honeybee navigation en route to the goal: visual flight control and odometry. J Exp Biol 199(1):237–244

Srinivasan M, Poteser M, Kral K (1999) Motion detection in insect orientation and navigation. Vis Res 39(16):2749–2766

van Hateren J, Schilstra C (1999) Blowfly flight and optic flow. II. head movements during flight. J Exp Biol 202(11):1491–1500
van Santen J, Sperling G (1985) Elaborated Reichardt detectors. J Opt Soc Am A 2(2):300–320
von Frisch K (1993) The dance language and orientation of bees. Harvard Univesity Press, Cambridge